A Fully Integrated Electronic-Photonic Platform for Label-Free Biosensing

Christos Adamopoulos
Vladimir Stojanovic, Ed.

Electrical Engineering and Computer Sciences
University of California at Berkeley

Technical Report No. UCB/EECS-2020-15
http://www2.eecs.berkeley.edu/Pubs/TechRpts/2020/EECS-2020-15.html

January 13, 2020

Acknowledgement

To begin, I would like to thank my advisor Vladimir Stojanovic for his continuous support throughout this project. None of this would be possible without him. I would like to thank him for his patience, his guidance and for always being there for me especially at the very beginning of my years at Berkeley. I would also like to thank my other two advisors, Professor Ali Niknejad and Professor Mekhail Anwar for always supporting me and giving me the best advice. Furthermore, I wish to thank my friend and collaborator in this project, Asmay Gharia as well as my wonderful ISG labmates. None of this would be possible without their precious help. Finally, I owe a special thanks to my family for always supporting me with their patience and love.

Contents

List of Figures

List of Tables

Acknowledgements

To begin, I would like to thank my advisor Vladimir Stojanovic for his continuous support throughout this project. None of this would be possible without him. I would like to thank him for his patience, his guidance and for always being there for me especially at the very beginning of my years at Berkeley. I would also like to thank my other two advisors, Professor Ali Niknejad and Professor Mekhail Anwar for always supporting me and giving me the best advice. Furthermore, I wish to thank my friend and collaborator in this project, Asmay Gharia as well as my wonderful ISG labmates. None of this would be possible without their precious help. Finally, I owe a special thanks to my family for always supporting me with their patience and love.

Abstract

Label free photonic sensors have shown increasing promise in monitoring molecular interactions. However, a system with full integration of the optical sensors together with a low noise readout and signal processing system in a high volume SOI process remains an unmet need. In this report we build a solid theoretical and experimental background for using the commercial CMOS 45nm RFSOI platform as a label free sensing process. In order to prove the feasibility of a fully integrated electronic-photonic platform for biosensing applications, the sensitivity of the platform is first characterized in Lumerical. A system level analysis is then presented by examining different photonic architectures using a Ring Resonator (RR) as a sensor. This report also addresses the challenges faced in creating a robust protein immobilization chemistry in 45nm process and efficiently delivering testing solutions using microfluidic channel networks. Finally, the capabilities of this platform are evaluated using RR filter banks, which include a sensing ring exposed to the testing solution and reference rings covered by PDMS for common mode error cancellation. The bulk sensitivity of the platform is demonstrated with different Refractive Index (RI) oils, while functionalized surface sensing sensitivity is evaluated with varying streptavidin concentration solutions flowing through a microfluidic channel. The analysis and results provided by this report open the pathway to the first Lab-on-Chip system with nanophotonic sensing and advanced electronics on a single die.

Chapter 1

Introduction

Affinity based biosensors are showing increasing importance in quantifying biological and biochemical processes. Several biosensing technologies have been introduced with high sensitivity that approach single molecule detection. However, most biosensors require a label attached to the target. The readout is indicative of the amount of label detected, which corresponds to the number of the target analytes bound on the sensor.

Label based sensing techniques, despite their high sensitivity, can have several disadvantages. Labeling can be an expensive and time consuming process interfering sometimes with the molecular event examined [1]. In order to address these challenges, an indirect label based technology is used, such as the ”sandwitch” Elisa [2], one of the most established assay platforms. The sensitivity achieved with this sandwitch assay is enhanced compared to the more simplified label based techniques, however it still carries several of the inherent bottlenecks of the labeling process.

One of the promising alternatives for affinity-based biosensors is label free sensing. In this technology, instead of tags, the readout signal is the result of a change in the intrinsic physical properties of the target analyte when it binds to the receptor molecules. Since there is no need for any complex labeling process, this technique can be cost effective and time efficient. At the same time, label free sensing allows monitoring the molecular interactions in real time providing

useful information about the affinity rate of the reaction under test and the dynamic interplay of molecules.

Several label free biosensing technologies have been introduced showing promising results in terms of sensitivity and speed. They can be divided into three main categories: mechanical electrical and optical bisosensors. The binding between target and receptor molecules can induce a change in the surface stress of a mechanical cantilever beam which is indicative of the amount of target molecules bound on the sensor [3]. In electrical label free sensors the binding events change the impedance between the electrode electrolyte interface [4, 5]. In this report, label free optical sensors will be examined.

1.1 Scope of Work

Evanescent field optical sensors based on resonant photonic structures [6, 7] have shown increasing promise in monitoring labeless molecular interactions. However, full integration of the biophotonic sensors together with a low noise readout and signal processing system in a high volume SOI process remains an unmet need. This technology will reduce cost and enable self-contained point-of-care devices that are needed in health-care applications. One strategy to enable this new class of systems-on-a-chip is to use monolithic integration of silicon photonics and advanced, high-performance CMOS transistors at a large scale and high yield [8]. In this technical report we first present a theorectical background of resonant photonic sensors in 45nm RFSOI platform and analyze different system architectures. At the same time, fabrication work on functionalizing the sensor and delivering fluids is shown before presenting the first label-free optical biosensing results utilizing ring resonators (RRs) in this commercial CMOS platform. This proves the main objective of this work, which is the feasibility of a fully integrated electronic-photonic platform for label-free sensing.

1.2 Organization

This thesis is organized as follows. In chapter 2, a widely used resonant photonic structure, the ring resonator is analyzed and some of its basic characteristics are introduced. The sensitivity of the device as a sensor as well as the overall effective sensitivity of a photonic system is defined. Furthermore, the potential of the 45nm CMOS platform as a label free sensing platform is investigated and characterized though simulations, using Lumerical.

In chapter 3, the basic categories of photonic sensing architectures are introduced and analyzed in terms of their complexity and sensitivity. Using ring resonators as the basic transducers, more advanced phase based photonic systems can be designed, less sensitive to power fluctuations. Based on the simulation results of chapter 2, the specifications of a system for monitoring real time kinetics are calculated.

In chapter 4, we emphasize on the interface between photonic sensors and biology. Specifically, the surface chemistry needed for label free sensing is presented and a simple applied chemical protocol for functionalizing the sensor will be analyzed. Verifying the functionality of the chemistry in our platform is a first promising step required to prove its feasibility for supporting label free sensing. In order to deliver the testing solution on the sensor an efficient microfluidic network is required. In this chapter two basic delivery mechanisms will be shown. The first one is based on the static delivery of droplets while the second scheme is dynamic and includes a microfluidic device built for one of the chips in 45nm process. The challenges faced for fabricating the fluidic delivery components will be analyzed.

Chapter 5 presents the first preliminary results of label free sensing in 45nm process. Bulk sensitivity results of ring resonators designed in 45nm SOI will be shown and compared to Lumerical Simulations. Real time kinetics of molecular interactions will also be presented for the first time in a fully integrated platform. This will set the basis for future work, which includes a first of its kind integrated label free system with photonic sensing and readout processing on the same die.

Chapter 2

Label Free Biosensing with Silicon Photonics

Silicon photonics is an emerging label free sensing technology offering several advantages in terms of size, efficiency and sensitivity. Due to its compatibility with CMOS processes, complex chip-scale photonic systems can be fabricated integrating multiple biophotonic sensors for multiplexed sensing. The silicon on insulator technology allows the large confinement of the optical mode. However, the evanescent tail of the electric field interacts with the cladding environment. This sets a unique opportunity for sensing any changes in the sensor's top surface. In this chapter the operating evanescent sensing principle will be presented. A widely used photonic structure, the Ring Resonator (RR) will be introduced as a biosensor in section 2.1 and the main design parameters will be analyzed. In section 2.2 the intrinsic sensitivity of the 45nm process as a label free sensing platform will be examined setting the basis for evaluating the system specifications in the next chapter.

2.1 Ring Resonators for Biosensing

Microring resonators have extensively been covered in literature [9]. The simplest form of a RR is an all pass topology, shown in Fig. 2.1.

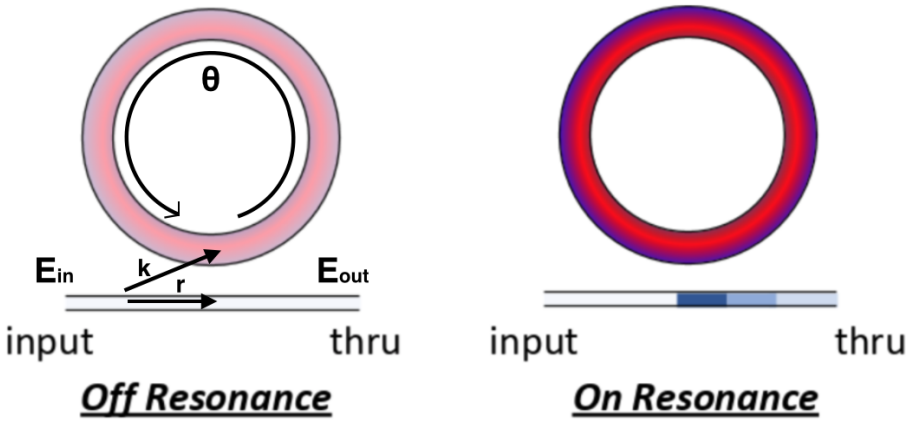

Figure 2.1: A RR consists of a bus coupled to a looped waveguide. The ring can be on or off resonance depending on the ratio of the wavelength λ to the optical round trip length L

It consists of a circular looped waveguide and an access waveguide to couple the loop. When the optical round trip length of the loop is equal to an integer multiple of the wavelength the RR is on resonance and most of the input power circulates in the ring. When the ring is off resonance then all of the input power passes to the thru port. The RR's spectrum is shown in Fig. 2.2. It consists of multiple resonances located at the resonant wavelengths λ_r , which are given by the following expression:

$$\lambda_r = \frac{n_{eff} L}{m} \tag{2.1}$$

where n_{eff} is the effective index of the optical mode propagating through the waveguide, L is circumference of the ring's circular loop and m is the integer number of times that the wavelength fits in the optical round trip length $n_{eff}L$. The spacing between consecutive resonances is

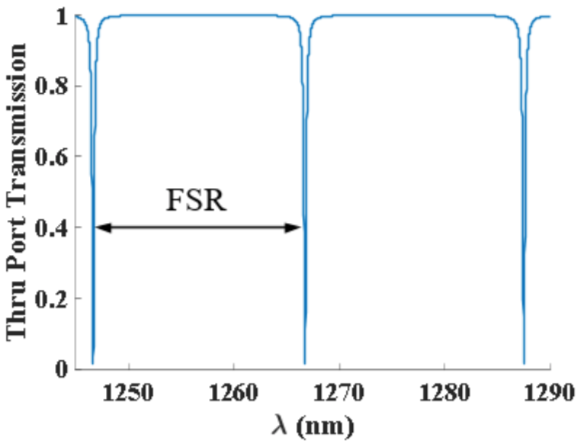

Figure 2.2: The spectrum of a RR consists of multiple resonances separated by the Free Spectral Range (FSR).

called Free Spectral Range (FSR) and is inversely proportional to the ring's radius. FSR can be quantitatively derived:

$$FSR = \frac{{\lambda_r}^2}{n_g L} \tag{2.2}$$

where group dispersion has been taken into account through n_g. The resonant spacing determines the dynamic range of a wavelength interrogation scheme as it will be shown in chapter 3. The thru port transfer function of an all pass RR can be derived as the ratio of the transmitted to the incident field of the bus waveguide [9]. It is a function of the self coupling coefficient r between the bus waveguide and the ring cavity, the round trip phase offset $\theta = \frac{2\pi}{\lambda} n_{eff} L$ and the single-pass amplitude transmission a:

$$t = \frac{E_{out}}{E_{in}} = \exp(i + \pi)\frac{a - re^{-i\theta}}{1 - rae^{i\theta}} \tag{2.3}$$

By squaring (2.3), the power transmission T_p can be derived as:

$$T_p = t^2 = \frac{a^2 - 2arcos(\theta) + r^2}{1 - 2arcos(\theta) + (ar)^2} \tag{2.4}$$

The sensitivity of a RR as a biosensor depends on the slope of the resonance shape. This can be quantified by the ring's quality factor Q, which represents the number of the oscillations that a photon undergoes inside the looped waveguide before it is lost to the surrounding medium. The larger the quality factor is the longer the lifetime of the photon, resulting to stronger interactions with the cladding environment. Translating its physical meaning to the spectrum domain, a large Q corresponds to a sharper ring's Lorentzian.

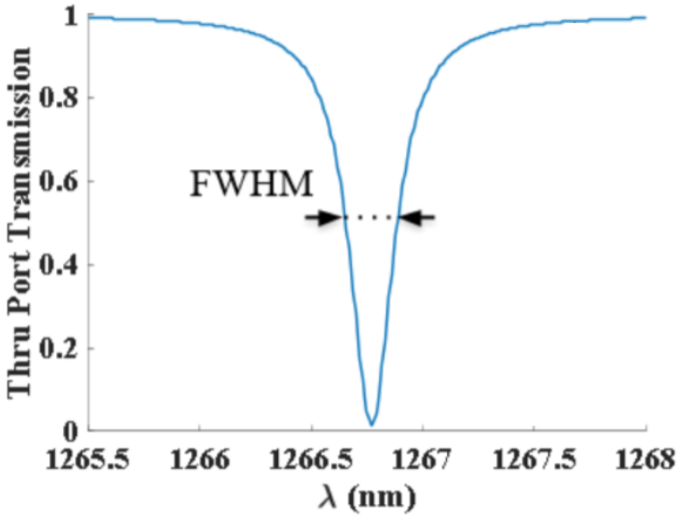

Figure 2.3: The quality factor Q of a RR affects the slope of the resonance shape.

Quality factor Q can be expressed as the ratio of the resonant wavelength λ_r to the RR's Full Width at Half Maximum (FWHM), which represents the bandwidth of the ring, as shown in Fig. 2.3. Therefore, we can write:

$$\begin{aligned} FWHM &= \frac{(1-ar){\lambda_r}^2}{\pi n_g L\sqrt{(ar)}} \\ Q = \frac{\lambda_r}{FWHM} &= \frac{\pi n_g L\sqrt{(ar)}}{(1-ar)\lambda_r} \end{aligned} \tag{2.5}$$

From the equation above, we understand that Q scales linearly with the ring radius as long as the propagation losses are not dominating. The spectrum in Fig. 2.3 shows a ring at critical

coupling. We use this term when the coupled power ($\sqrt{1-r^2}P_{in}$) is equal to the power loss inside the ring. In this mode of operation the power at the thru port is zero. For a self coupling coefficient $r < a$ the ring is overcoupled whereas for $r > a$ the ring is in the undercoupled region. A more detailed analysis about the sensitivity optimization of the resonant shape will follow in the next chapter.

From the figures above, it is clear that the resonance shape has a strong impact on how sensitive a ring is. A small wavelength shift can be more easily detectable in a high Q ring, since the dT_p of the transmission coefficient at a fixed wavelength will result to a larger dP power change at the thru port compared to lower Q ring. However, it is critical to understand how large this wavelength shift can be for any environmental changes. In other words, if we descend one level below in the hierarchy, sensitivity is also affected by the amount of the effective index change from environmental factors, since this determines the wavelength shift. Therefore we can define two different types of sensitivities. Using the expression for the resonant wavelength, while taking into account dispersion [10] the intrinsic sensitivity can be given by:

$$S_{int} = \frac{\Delta\lambda}{\Delta n_{clad}} = \frac{\partial n_{eff}}{\partial n_{clad}} \frac{\lambda_r}{n_g} \tag{2.6}$$

where n_{clad} is the cladding refractive index. This type of sensitivity describes the amount of wavelength shift $\Delta\lambda$ of a RR that would result from a refractive index change in the cladding environment, Δn_{clad}. This environmental change affects the effective index n_{eff} of the ring's waveguide, which in turn results to a wavelength shift. The intrinsic sensitivity of a ring can be characterized though waveguide simulations as shown in the next section.

The second type sensitivity depends on the sharpness of the resonance shape. A ring with a larger quality factor Q will be characterized by a sharper resonant slope. At a fixed wavelength λ, this can qualitatively be translated to a larger power fluctuation dP_{out} at the thru port of the ring if a wavelength shift occurs. Therefore, this type of sensitivity, denoted as S_{ring} can be given by:

$$S_{ring} = \frac{\partial P_{out}}{\partial \lambda} \tag{2.7}$$

If we take both sensitivities into account we can define the overall effective sensitivity,

$$S_{eff} = S_{ring} * S_{int} \tag{2.8}$$

One the most critical figure of merits for a biosensor is the limit of detection (LOD), which describes the minimum measurable quantity that can be detected by the transducer. It is clear that the LOD depends on the minimum resolvable wavelength shift and the overall sensitivity previously defined. In order to define a LOD that does not depend on the measurement setup, it can be assumed that the minimum resolvable wavelength shift is equal to the FWHM of the ring [11]. A ring with a large quality factor results to a smaller FWHM, thus a smaller minimum resolvable shift and vice versa. The LOD can then be defined as:

$$LOD = \frac{FWHM}{S_{int}} = \frac{\lambda_r}{QS_{int}} \tag{2.9}$$

From the above expression, a RR with a large Q is desired. This will lead to a sharper resonant slope therefore increasing the change in the output power of the ring for a given resonant wavelength shift and resulting to a smaller minimum resolvable wavelength shift.

2.2 CMOS 45RFSOI as a Biophotonic Platform

The first step for characterizing the sensing performance of a photonic transducer is to examine the intrinsic sensitivity of the device. This strongly depends of the waveguide geometry and the integrated process. The interaction of the evanescent field of the mode and the cladding environment determines the change in the effective index Δn_{eff}, which can then be translated to other parameters, depending on the type of the photonic sensor.

The cross section of a waveguide in 45nm RFSOI process is shown in Fig. 2.4. Undoped Si-crystalline transistor body is used as the waveguide layer. The thin Buried Oxide layer (BOX) in

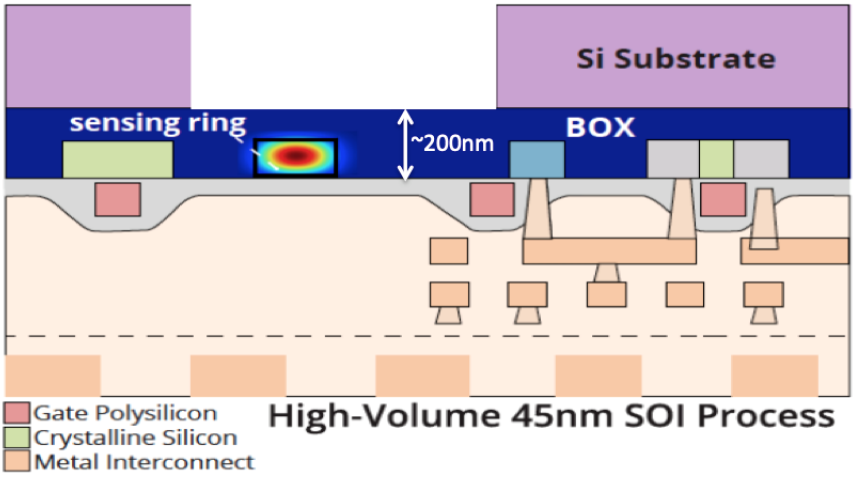

Figure 2.4: CMOS 45RFSOI process cross-section. The thin Si-body waveguide layer allows a low confinement of the optical mode. Backside substrate etch exposes the sensing area.

this advanced process node requires Si substrate release to prevent leakage of the waveguide mode into the silicon substrate. This creates a unique opportunity for photonic sensor design due to the relatively low confinement of the optical mode in the thin waveguide and BOX layers, resulting in a strong evanescent field interaction with any material above the BOX layer. This interaction can be further enhanced with a partial etch of the BOX layer as it will be shown in this section.

In order to evaluate the label free sensing performance of our platform two basic simulation setups were examined. In Fig. 2.5 the bulk sensitivity of the platform is characterized. To this end, the RI of the cladding material above the BOX is swept and the resonant shift of a default 5um radius RR is calculated using (2.1). The surface sensing performance of the process is evaluated by sweeping the thickness of a layer of a specific RI on top of the BOX (2.5b). This layer can model the binding events taking place on top of our sensor, therefore we can assign the RI of a protein (1.45) to it. A surface sensing sensitivity expressed in $\frac{shift}{thickness}$ units can be determined. This can allow us to estimate the effect of single molecular binding events. All simulation results shown are derived using Lumerical.

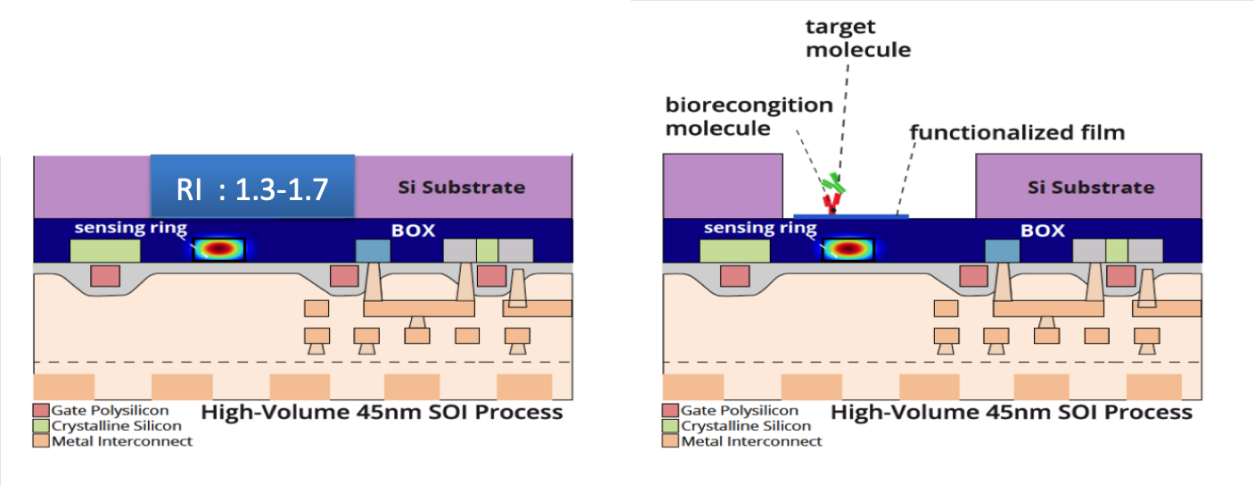

(a) (b)

Figure 2.5: (a) Bulk sensing simulation setup. The RI of the cladding material is swept to model the effect of a different background solution on top of the sensor. (b) Surface sensing simulation setup. A thin layer with variable thickness models the binding events between receptor and target molecules taking place on top of the BOX.

The waveguide geometry determines the confinement of the optical mode. For biosensing applications a low mode confinement is desired that can result to stronger interaction with any environmental change in the cladding environment. As the thickness and width decreases, the mode is less confined leading to stronger interactions. However this can lead to higher losses resulting to a lower Q ring and a lower effective sensitivity for the device. For a waveguide thickness of 70nm and a width of 1.2um, bulk sensitivity is first evaluated, as shown in Fig. 2.6.

This metric of performance can give us useful feedback about the effect bulk environmental changes could have on our sensor. Additionally, we can estimate the offset changes induced by the background solutions containing the target analytes. A bulk sensitivity of $5\frac{nm}{RIU}$ is simulated. This results to an offset shift of $2nm$ when the sensor is exposed from air to water, which is the buffer solution for most testing fluids. A reduced BOX thickness can significantly boost the sensitivity (Fig. 2.6). This can be explained from the lower mode confinement leading to stronger interactions with the cladding environment. A 100nm etch is expected to increase by x7 the bulk sensitivity.

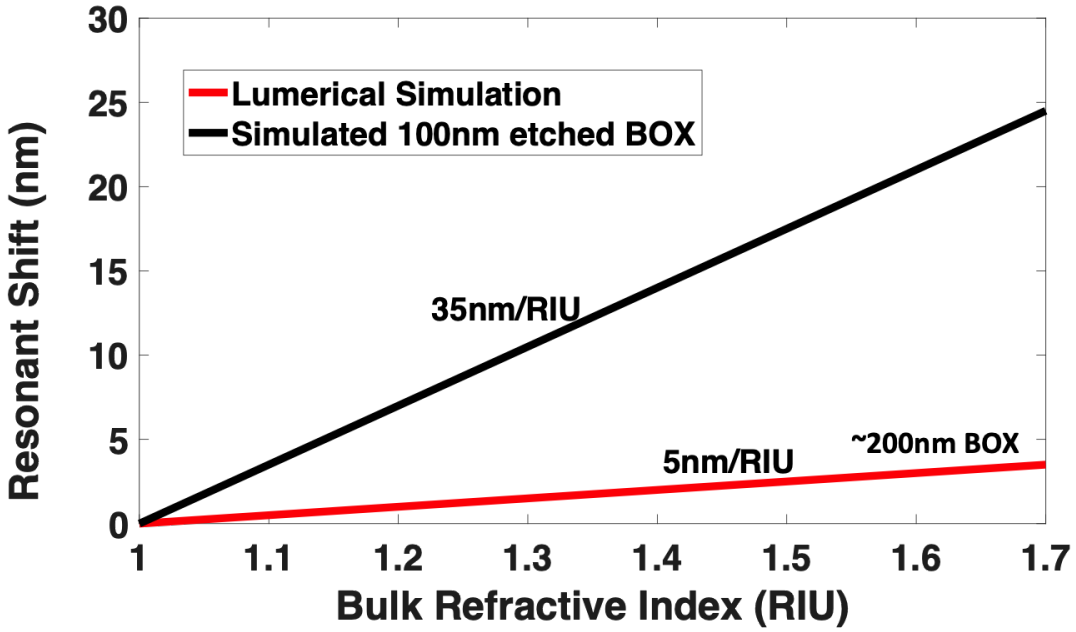

Figure 2.6: The bulk sensitivity of the 45nm process is evaluated. The resonant shift of a 5um default RR is calculated for different RI values of the cladding environment. A boost in sensitivity can be achieved with a reduced BOX thickness.

In Fig. 2.7 the surface sensing performance of the 45nm platform is examined. Translating the change in the effective index to a resonant shift of a 5um radius RR, a sensitivity of $33\frac{pm}{nm}$ is found. A uniform 10nm molecular layer over the ring resonator would result to a 300pm resonant shift, which corresponds to approximately twice the bandwidth of the ring (11GHz).

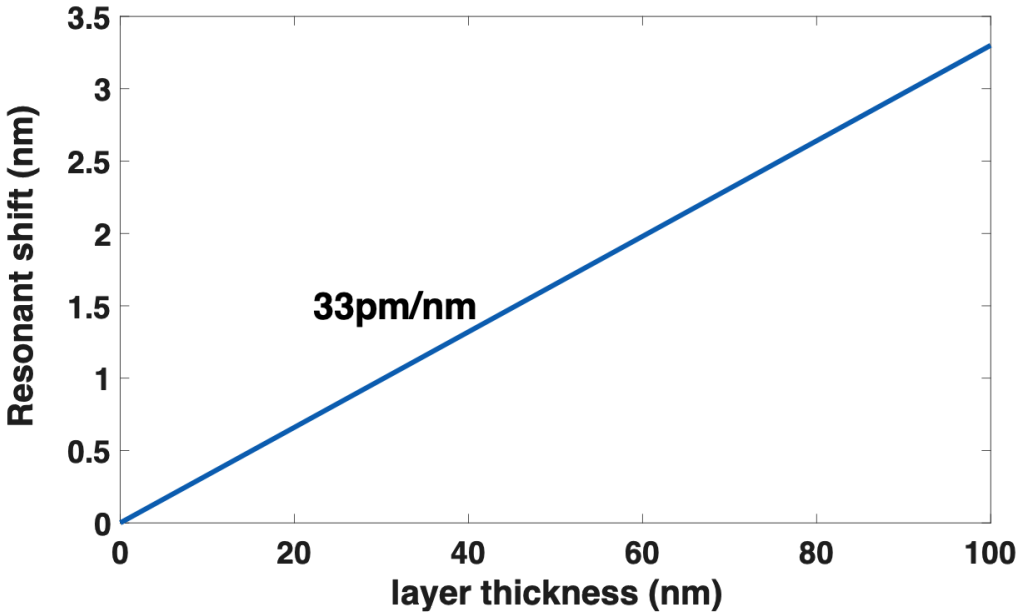

Figure 2.7: The surface sensitivity of the 45nm process is evaluated. The thickness of a thin layer on top of the BOX is varied resulting to a change in the effective index and a resonant shift of a 5um RR.

In this section, two basic sensing modes of a photonic platform were characterized. Bulk and surface sensing are operating in parallel. A testing solution will have a background RI, resulting to a large offset wavelength shift. However, it also carries the analytes binding on the sensor, giving us the fine shifts related to surface sensing. As a final note, using our knowledge from the surface sensing characterization, we can attempt to estimate the effect of a single molecular binding event. In order to make this approximation, we can assume a default waveguide where the shape of the optical mode is localized at the center. This leads to two extreme scenarios regarding the effect of a binding event. The stronger interaction occurs when the molecular binding takes place at the center of the waveguide. However, if we consider a binding event happening at the edge of the waveguide where the evanescent tail of the mode is weak, we can extract an average value for the change of the effective index, Δn_{eff}, as shown in Fig. 2.8.

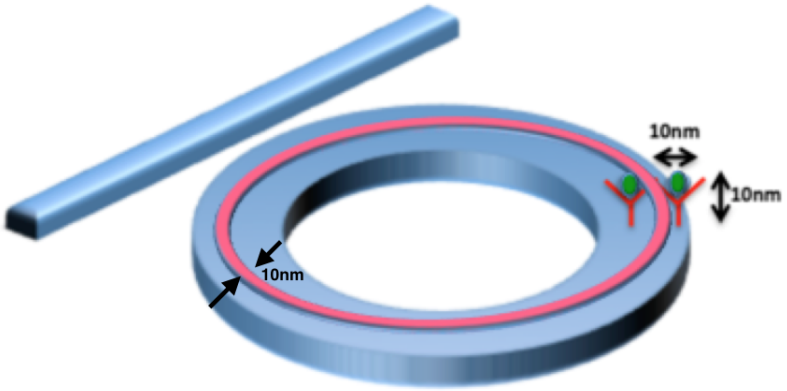

Figure 2.8: The effect of a single molecular binding is approximated by considering an average Δn_{eff} based on the location of the molecule.

In order to model the effect of a single molecule we assume for simulation purposes a 10nm default size of a large protein. The average change of the effective index from a 10nm wide and thick uniform layer all over the ring is first simulated (Fig. 2.8). By normalizing this result to the total perimeter L_{ring} of the ring, the effect from the 10nm cube can be approximated. Specifically,

$$\Delta n_{eff_{molecule}} = \frac{10nm}{L_{ring}} \Delta n_{eff_{\text{10x10nm layer}}} \approx 1nRIU \implies 0.6fm \implies 110kHz \tag{2.10}$$

This frequency shift corresponds to about 0.002% of the ring's FWHM. Even though detecting signals of this order remains a big challenge with conventional equipment, being able to determine the limits of our platform is necessary in order to set the design specifications of future systems.

Chapter 3

Photonic Sensing Architectures

A number of publications have proposed label-free biophotonic sensing based on resonant photonic structures [12, 13, 14, 15, 16, 17]. However, all of these techniques utilize passive photonic chips and devices and rely on complex external equipment and tunable lasers for precise optical optical spectrum scanning. This in turn limits the rate and accuracy at which measurements can be taken, and leaves the Q-factor of the photonic device as the only parameter through which a higher fidelity resolution can be achieved - striving towards a single molecule binding event detection. Optical spectrum curve fitting is used to enhance the resolution allowing a minimum resolvable wavelength lower than the linewidth of the laser source. The dynamic range of this interrogation scheme is equal to the FSR of the ring.

Specifically, the tunable laser technique listed in prior work, performs multiple scans of the whole thru-port transfer function and uses least-squares fitting to estimate the amount of wavelength shift and therefore the change in index of refraction and the rate of molecular binding. Due to limited speed of the tunable lasers, these techniques take minutes to perform a single estimation, and cannot perform a lot of averaging due to a limited number of data points that can be acquired in that time interval. As such, the method solely relies on the Q factor of the resonator as the means to improving the fidelity of the measurement. With Q-factors of less than 100,000 [6], these systems

have a resolution several orders of magnitude coarser than needed for single molecule detection. Second, the system has a narrow dynamic range since the sensitivity is tied to the scanning time, while the concentration of the target molecules determines the binding rate.

By leveraging our technology, which offers significant electronic resources tightly integrated on the same chip with photonic devices, we aim to create a single-chip system that will utilize the on-die electronics to eliminate the need for complex external equipment and also improve the fidelity and speed of the measurement. In this chapter, various photonic sensing architectures will be reviewed and analysed in terms of their sensitivity and complexity. These photonic front ends are compatible with a fixed wavelength scheme.

3.1 Intensity Interrogation Scheme

3.1.1 Single Ring Resonator

Monitoring the intensity fluctuations from resonant shift at a fixed wavelength allows the replacement of the tunable laser with more simplistic light sources and offers the possibility for precise tracking of fast molecular dynamics. As it was explained in Ch. 2, any molecular interaction occurring at the top of the BOX will result to a change in the effective index n_{eff} of the mode. This will induce a change in the round trip offset θ of the electric field in the ring. At the same time, Δn_{eff} will result to a wavelength shift $\Delta\lambda$ given by (2.1).

For a fixed wavelength scheme, this wavelength shift will result to a power fluctuation at the thru port of the RR, as shown in Fig. 3.1.

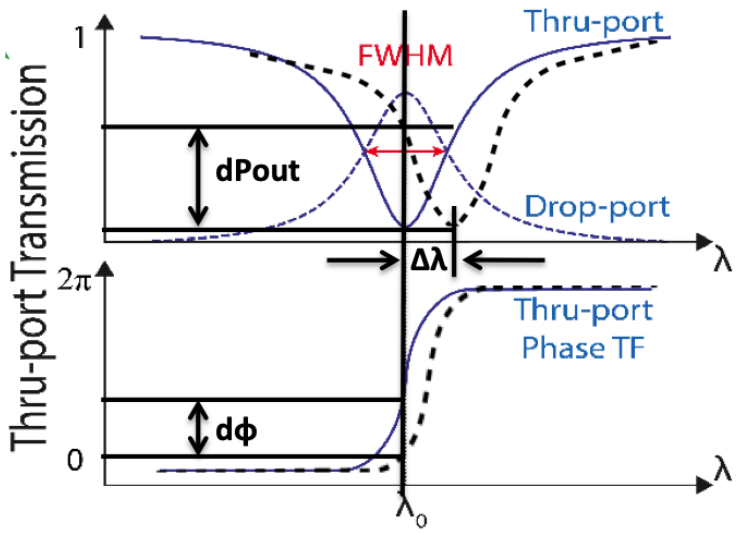

Figure 3.1: A wavelength shift $\Delta\lambda$ leads to power fluctuations dP_{out} at the thru port of a RR in a fixed wavelength scheme.

The scope of this chapter is to examine and optimize the sensitivity of a single ring. Furthermore, other photonic sensing architectures employing both amplitude and phase information will be reviewed and compared in terms of sensitivity and complexity. The last section will introduce some pure phase detection schemes, which show less sensitivity to any power fluctuations.

In order to evaluate the sensitivity of a RR, the slope of the Lorentzian shape needs to be analyzed. From (2.4) the output power is given by:

$$P_{out} = T_p P_{in} = t^2 P_{in} = \frac{a^2 - 2arcos(\phi) + r^2}{1 - 2arcos(\phi) + (ar)^2} P_{in} \tag{3.1}$$

A change in the n_{eff} results to a round trip phase change $\delta\theta$. Therefore, taking the derivative of P_{out} in terms of θ and normalizing it to the input power Pin, the normalized sensitivity S_{norm} of a single RR can be obtained:

$$S_{norm} = \frac{\partial P_{out}}{\partial \theta P_{in}} = \frac{a^2 - 2arcos(\phi) + r^2}{1 - 2arcos(\phi) + (ar)^2} P_{in} \tag{3.2}$$

The slope of the Lorentzian depends on the bias point θ at which the RR is operated and the self coupling coefficient r. Having these two design parameters as tuning knobs, the resonant shape can be optimized such that the slope from equation (2.4) is maximized for the optimal θ and r. In this analysis, the field loss coefficient is assumed to be 3.45/cm.

Even though an analytical expression for S_{norm} is obtained, a numerical evaluation of the sensitivity is carried out. Specifically both r and θ are swept over a wide range covering all coupling modes of the RR. In Fig. 3.2. each curve corresponds to a different value of self coupling coefficient r. The optimal bias point corresponds to approximately $10mrad$ off resonance round trip phase offset. For this $\theta_{optimal}$, r is swept in a range of $[0.7 - 0.999]$. The maximum S is obtained for a vlaue of $r > r_{critical}$ which indicates that the optimal sensitivity of the ring occurs in the undercoupled region. However, this direct intensity detection scheme does not employ any phase information of the electric field at the output port of the RR.

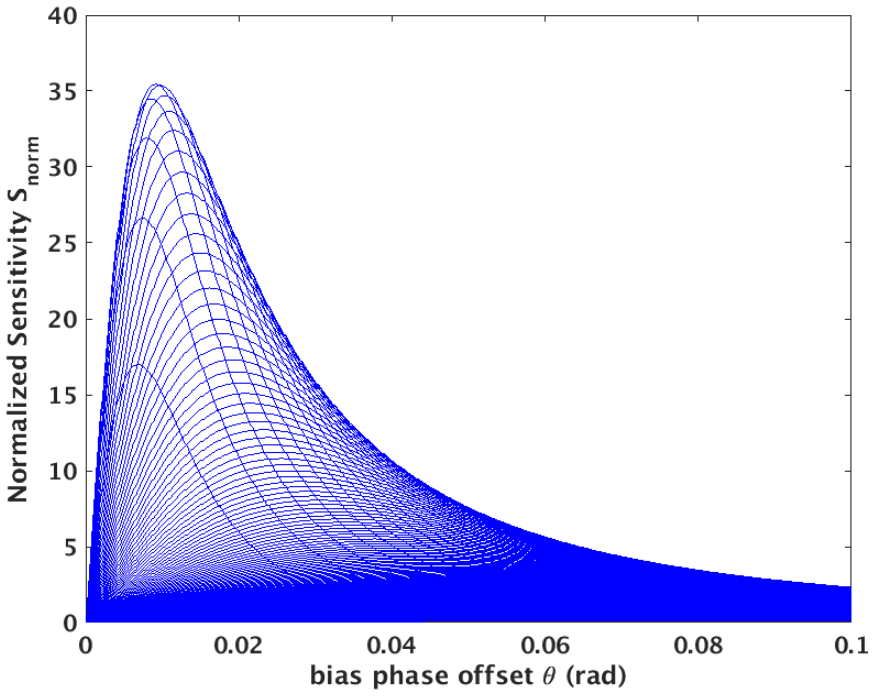

Figure 3.2: Normalized sensitivity of a single ring for a varying bias phase offset θ and self coupling coefficient r.

3.1.2 Ring Assisted Mach Zender Interferometer (RAMZI)

An architecture based on both amplitude and phase information is the RAMZI shown in Fig. 3.3.

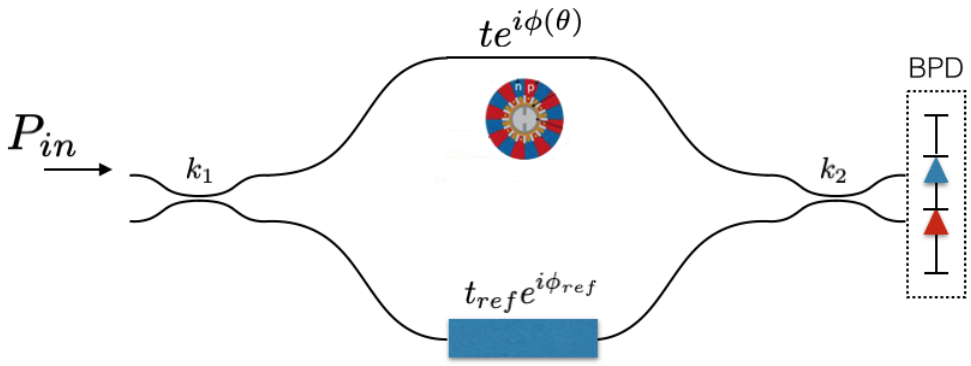

Figure 3.3: A Ring Assisted Mach Zender Interferometer.

Light of wavelength λ is launched into the input port of the device, where it is split into the two arms of Mach Zender Interferometer (MZI) by a first coupler with a power coupling ratio k_1. The sensing arm consists of a RR exposed to the environmental changes while the reference arm is used for offset calibration. The two arms are then reconnected by a second coupler of a splitting ratio k_2. P_1 and P_2 is the power at the output ports of the coupler. In this scheme, the power difference dP_{out} is detected. This is achieved by using a Balanced Photodetector (BPD) configuration, shown in 3.3. where the output current signal is proportional to the power difference $P_1 - P_2$, which depends on both the amplitude and phase slope of the output electric field of the RR.

In order to analyze the performance of the RAMZI, the sensitivity needs to be defined and optimized similarly to a single RR. Based on the analysis from [18] the normalized to the input power P_{in} sensitivity is given by:

$$
\begin{aligned}
S_{norm} = -(4Acos(\phi_{ref} - \phi(\theta)) + 2Bt(\theta))t'(\theta) - 4Asin(\phi_{ref} - \phi(\theta))t(\theta)\phi'(\theta) \\
A = \sqrt{k_1 k_2 (1-k_1)(1-k_2)} \\
B = k_1 + 2k_2 - 2k_1 k_2 - 1
\end{aligned}
\tag{3.3}
$$

where θ and t_{ref} is the ring's round trip phase shift and the amplitude coefficient of the reference waveguide respectively, ϕ is the output phase transfer function of the ring and ϕ_{ref} is the offset phase shift from the reference arm.

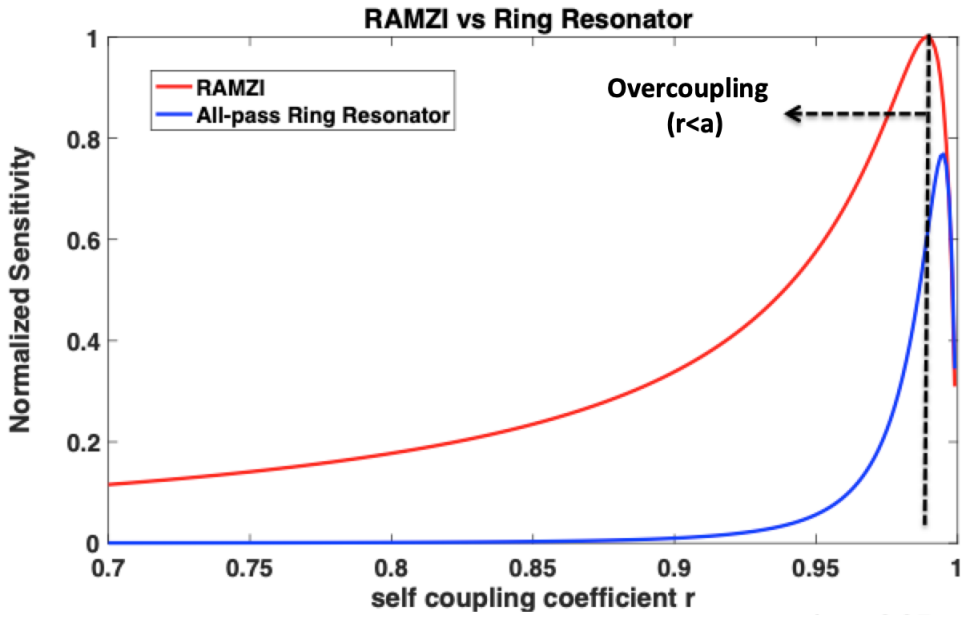

Figure 3.4: Normalized sensitivity vs self coupling coefficient r for a ring and a RAMZI at their optimal bias point θ_{opt}.

Compared to a single RR, optimization of the RAMZI structure includes more tuning knobs. The power splitting ratio of the input and output coupler can be first optimized. By taking the derivative of S_{norm} in terms of k_1 and k_2 the optimal splitting ratio can be found to be $k_1 = k_2 = 0.5$. In order to maximize S_{norm}, we need to optimize for θ and r. Both design parameters are swept in a wide range similar to the single ring analysis. First, the optimal bias phase point is determined by sweeping θ for different values of r. The maximum absolute sensitivity is found to be on resonance. For that bias point the self coupling coefficient is then swept in the same range of $[0.7 : 0.999]$. In Fig. 3.4, the normalized sensitivity of both a single ring and a RAMZI are shown. It can be observed that for a RAMZI structure the optimal slope occurs on resonance at critical coupling ($r = r_{critical}$), whereas for a ring the maximum sensitivity is found to be in the undercoupling region. In the overcoupling regime the RAMZI structure can be much more

sensitive than a single RR even though the absolute sensitivity is lower than the maximum point at critical coupling [18].

The sensitivity analysis presented in this section can help us quantify the effect of a single molecular binding event on a RR. In light of the previous results in Chapter 2, the Δn_{eff} from one molecule can be translated to a $d\theta$ of the ring's round trip phase shift. Using the S_{norm} sensitivity analysis of this section, the output power fluctuation dP_{out} at the thru port can be determined as a result of a single binding event. Assuming a default photodetector with responsivity $R = 0.5\frac{A}{W}$, the minimum photocurrent change di_{out} can be estimated. Being able to approximate the minimum signal will help us set the specifications for the readout circuitry. A detailed circuit level noise analysis is needed in order to characterize the Minimum Detectable Signal (MDS). This will indicate the required Signal to Noise Ratio (SNR) enhancement in order for a single binding event current change to be larger than the integrated noise at the circuit's input. For this system level analysis, we assume an input power of $P_{in} = 0dBm$ incident to a 5um radius ring with a quality factor of 10k. The maximum absolute sensitivity for this ring is approximately $30\frac{1}{\text{rad}}$. Therefore, the current change can be given by:

$$di_{out} = RdP_{out} = RP_{in}S_{norm_{ring}}d\theta = 0.5\frac{A}{W} * 1mW * 30\frac{1}{rad} * \frac{2\pi L_{ring}dn_{eff}}{\lambda} \approx 3nA \quad (3.4)$$

We should note, however, that this minimum signal can be significantly increased. By taking into account the $x7$ boost in intrinsic sensitivity due to the BOX etching, along with 200k higher quality factor rings previously demonstrated in this platform [19], a x140 SNR enhancement can be obtained.

3.2 Phase Detection Schemes

In order to achieve phase modulation two basic techniques can be employed. As it is shown in Fig. 3.5, light of wavelength λ entering the sensing arm is first phase shifted from a RR due to

the targeted molecular interactions. The electric field is then phase modulated by an SSB (Single Sideband) or a Serrodyne modulator. Both of these architectures eliminate one sideband allowing a phase-modulated photocurrent after the balanced photodetector. The nature of this signal ensures higher robustness to any power fluctuations occurring from the laser or from any mechanical vibrations in the fiber to chip interface.At the same time, modulating the electric field allows low frequency noise suppression, thus reducing the integrated noise power and lowering the MDS.

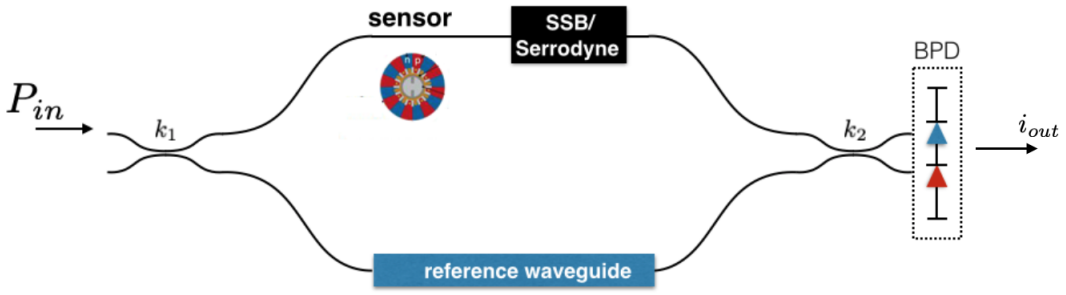

Figure 3.5: A phase detection architecture. Elimination of one of the sidebands using an SSB or a serrodyne modulation scheme results to a purely phase modulated photocurrent.

A brief overview of each of these techniques will be presented and some basic $FOMs$ will be introduced to evaluate their relative performance.

3.2.1 Single Sideband Modulation (SSB)

Figure 3.6 shows the basic architecture of an SSB modulator. It consists of two nested Mach Zender Modulators (MZM) driven by two orthogonally ($\Delta\phi = \frac{\pi}{2}$) sine waves. The modulated electric field at the output of the upper MZM is given by:

$$E_A = \frac{E_{in}}{\sqrt{2}} e^{\frac{2\pi n_0 L_{arm}}{\lambda}} cos(\frac{\pi S}{S_\pi} cos(\omega_m t)) cos(\omega_0 t) \tag{3.5}$$

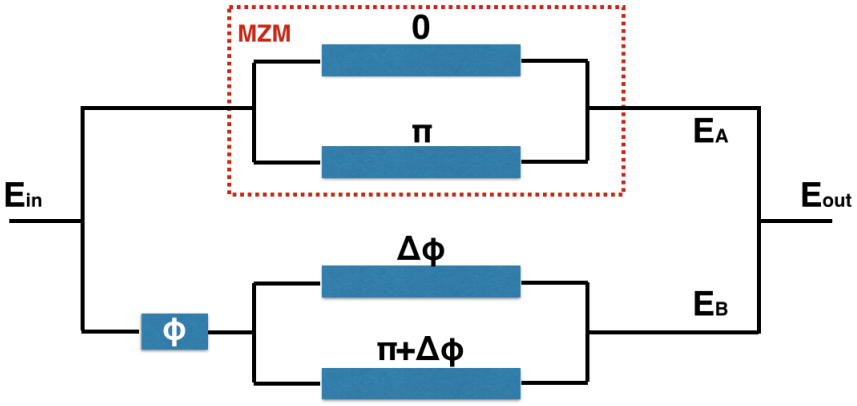

Figure 3.6: A Single Sideband Modulator.

where S is the modulation signal, L_{arm} is the length of the MZM's arm, n_0 is the nominal effective index of the waveguide without any modulation, ω_m and ω_0 are the modulation and carrier frequency respectively and S_π is the signal needed for a π phase shift. It should be noted that depending on the type of modulation, the driving signal S can take various forms. As an example, we can consider two different types of modulation, electrooptic and thermooptic. In the fist case, a voltage V changes n_{eff} based on the electrooptic effect [20], whereas in thermooptic modulation the power P_{heat} heating the waveguide changes n_{eff} based on the thermooptic coefficient of the materials. Assuming that a first order approximation of the effective index is given by $n_{eff} = n_0 + pS$, where p is the modulation efficiency, S_π can be derived as follows:

$$S_\pi = \frac{\lambda}{2pL_{arm}} \tag{3.6}$$

If the modulation signal S consists of a dc and an ac component we can write:

$$
\begin{aligned}
S &= S_{dc} + s_{am}cos(\omega_m t) \\
E_A &= \frac{E_{in}}{\sqrt{2}}cos(\frac{\pi S_{dc}}{S_\pi} + \frac{\pi s_{am}}{S_\pi}cos(\omega_m t))cos(\omega_0 t + \frac{2\pi n_0 L_{arm}}{\lambda}) \\
E_B &= \frac{E_{in}}{\sqrt{2}}cos(\frac{\pi S_{dc}}{S_\pi} + \frac{\pi s_{am}}{S_\pi}cos(\omega_m t + \Delta\phi))cos(\omega_0 t + \frac{2\pi n_0 L_{arm}}{\lambda} + \phi)
\end{aligned}
\tag{3.7}
$$

where $\Delta\phi = \frac{\pi}{2}$ since the two MZMs are driven orthogonally and ϕ is the phase offset in the bottom arm of the SSB. By combining the output fields E_A and E_B we can derive the following expression for the output field E_{out}:

$$
\begin{aligned}
E_{out} = \frac{E_{in}}{2}J_1(\frac{\pi s_{am}}{S_\pi})(cos(\omega_m t)cos(\omega_0 t + \frac{2\pi n_0 L_{arm}}{\lambda}) + \\
+cos(\omega_m t + \Delta\phi)cos(\omega_0 t + \frac{2\pi n_0 L_{arm}}{\lambda} + \phi)) + \text{higher order terms}
\end{aligned}
\tag{3.8}
$$

where J_1 is the 1^{st} order Bessel function and E_{in} is the input electric field. If the phase offset ϕ in the bottom arm is $\frac{\pi}{2}$ or $-\frac{\pi}{2}$ then one of the two sidebands, $\omega_0 + \omega_m$ or $\omega_0 + \omega_m$ respectively is eliminated. The phase detection architecture of Fig. 3.5 uses an SSB as a building block in the sensing arm next to the RR. The output photocurrent i_{out} after the balanced photodetector is given by:

$$
i_{out} = RP_{in}f(k_1, k_2)cos(\omega_m t + \delta\phi_{sense} + \phi_{offset}) \tag{3.9}
$$

where R is the responsivity of the balanced PD, $f(k_1, k_2)$ is a function of the input and output coupler splitting ratio, $\delta\phi_{sense}$ and ϕ_{offset} are the sensing and offset phase respectively and P_{in} is the laser's input power. As we can observe, the detected current signal is a purely phase modulated current that embeds the phase changes from the molecular interactions inside the phase of the sinewave. This is achieved from the SSB by eliminating one of the sidebands. The basic FOMs used in order to evaluate the performance of these phase modulation techniques are the sideband suppression ratio (SR) and the total harmonic power. One of the main characteristics of an ideal SSB is the perfect cancellation of one sideband regardless of the modulation depth of the MZMs. However, several non idealities depending on the modulation scheme (AM-PM distortion

in electrooptic modulation) can degrade the SR. One of the main disadvantages though of an SSB scheme is the increased harmonic power for decreasing modulation depth resulting to a large insertion loss. Let h_i be the harmonic power of the i^{th} tone, $\omega_0 + i\omega_m$. Based on the Bessel expansion analysis, the ratio between different harmonic tones can be found analytically. If we assume a driving modulation signal $S = S_{dc} + s_{am}cos(2\pi f_m t)$, we can write:

$$\begin{aligned} \frac{h_1}{h_{n_{even}}} &= \frac{sin(\frac{\pi S_{dc}}{S_\pi})J_1(\frac{\pi s_{am}}{S_\pi})}{cos(\frac{\pi S_{dc}}{S_\pi})J_{n_{even}}(\frac{\pi s_{am}}{S_\pi})} \\ \frac{h_1}{h_{n_{odd}}} &= \frac{J_1(\frac{\pi s_{am}}{S_\pi})}{J_{n_{odd}}(\frac{\pi s_{am}}{S_\pi})} \end{aligned} \tag{3.10}$$

As it was previously derived, the even harmonics including the carrier frequency can be eliminated for a dc component equal to $S_{dc} = \frac{S_\pi}{2}$.

3.2.2 Serrodyne Modulation

An alternative architecture to the SSB scheme is serrodyne modulation. One of the advantages of this scheme is the smaller level of complexity, since the core structure consists of a single phase shifter. The key principle is the modulation of the phase shifter by a sawtooth waveform (3.7), resulting to a linearly increasing phase in the time domain and therefore a frequency shift equal to the modulation frequency, $\frac{1}{T_{mod}}$.

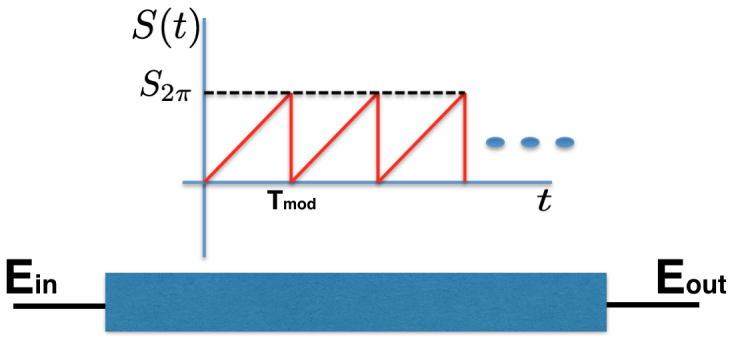

Figure 3.7: A Serrodyne Modulator driven by a sawtooth waveform with a peak value of $S_{2\pi}$.

The peak value of the sawtooth is equal to $S_{2\pi}$. Therefore, the linear segment of the driving signal can be written as:

$$S(t) = \frac{S_{2\pi}}{T_{mod}} t \tag{3.11}$$

The electric field at the output of the phase shifter can be given by:

$$\begin{aligned} E_{out} = E_{in} e^{\frac{2\pi n_0 L_{arm}}{\lambda}} cos(\omega_0 t + \frac{2\pi p L_{arm}}{\lambda} S(t)) = \\ = E_{in} e^{\frac{2\pi n_0 L_{arm}}{\lambda}} cos(\omega_0 t + \frac{\pi}{S_\pi} S(t)) = E_{in} e^{\frac{2\pi n_0 L_{arm}}{\lambda}} cos(\omega_0 t + \frac{2\pi}{T_{mod}} t) \end{aligned} \tag{3.12}$$

One of the critical aspects of serrodyne modulation is the peak value of the sawtooth waveform. In the ideal case, a $S_{2\pi}$ is required in order to perfectly cancel one of the sidebands. However, being able to generate a full $S_{2\pi}$ is not always a trivial task, mainly because it can lead to unrealistically lengthy components for an integrated system. Therefore, it is important to quantify the effect of a reduced swing on the SR. Another challenge that we need to face in a serrodyne modulation scheme is the finite fall time of the sawtooth waveform due to the limited bandwidth of the driver generator. The effect of both of these non idealities on the SR can be shown in Fig. 3.8.

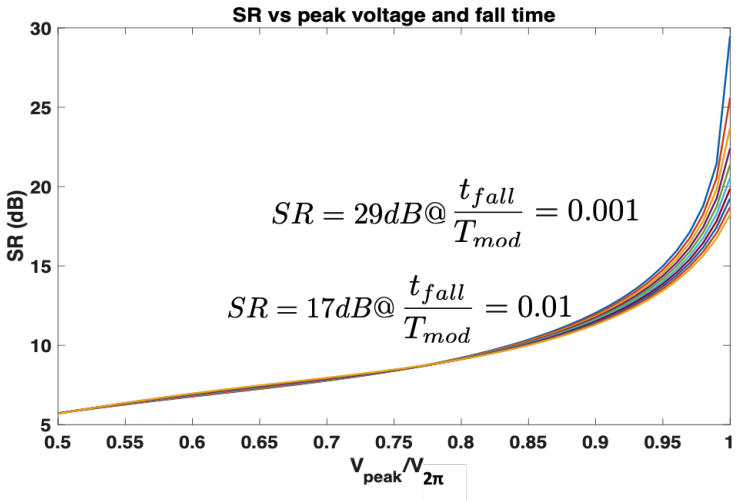

Figure 3.8: The peak value of the sawtooth waveform and its finite fall time can severely degrade the Sideband Suppression Ratio (SR).

Chapter 4

Surface Chemistry and Fluidic Delivery

4.1 Functionalization and Protein Immobilization

One of the most critical parts of a biosensing platform is the interface between the transducer and the biological target analyte. Key for detecting very low concentrations of molecules is a robust interface between the testing solution and the photonic sensor. In affinity based sensors, the biorecognition molecules need to be immobilized at the sensor's surface in order to bind with the target analytes in the testing solution. A wide variety of functionalization protocols have been used in label fee sensors. One of the key challenges in this project was to verify that our electronic photonic platform is compatible with the state of the art cost effective functionalization protocols. The Si substrate release needed for preventing any leakage of the waveguide mode into the substrate, could potentially interfere with any surface chemistry for protein immobilization. Therefore, being able verify the functionality of a simple protocol in our process is an important step.

The surface chemistry applied in Si based label free sensors is based on silane reagents that can have a wide range of functional groups. This allows the efficient coupling of the receptor molecules to an aminosilane layer formed on top of the sensors, which can then allow the specific

label free binding of the target molecules. As a proof of concept for functionalizing the sensor's surface in 45nm process, the gold standard of avidin biotin was used. The extremely large affinity of avidin for biotin can allow safe conclusions regarding the efficiency of the surface chemistry. For that reason, the same pair was used for the real time kinetic measurements, presented in the next chapter.

Biotin is a vitamin found in all living cells with a mass of about 244 Da. It is widely used in increasing the sensitivity of many assays since it can be conjugated to many proteins. Avidin is a glycoprotein with a mass of approximately 68 kDa. There are four identical subunits where one biotin protein can bind. Since the top surface of our sensors is a SiO2 BOX layer, the protocol verification experiments were performed with glass slides. Biotin is immobilized on the glass slide's surface as a receptor molecule and streptavidin is the target analyte in the sample solution.

As a first step, the glass slide was dip coated for 3mins in a 2% APTES-ethanol solution in order to be functionalized with aminosilane groups. A uniform APTES layer of about 5-10nm thickness is expected to form on top of the slide. This existence of this layer is verified though a static shift in the coated rings. Immobilizing biotin receptor molecules on the sensor's surface was verified using a fluorescent microscope. Specifically the binding between biotin and streptavidin is visualized under a FITC fluorescent microscope. The APTES coated glass slide was first spotted with biotin drops and left overnight in a cool environment. Then after washing off the glass slide, a large drop of streptavidin conjugated with Alexa fluorophore was spotted. Using a FITC filter, the glass slide was excited with the fluorophore's excitation wavelength of 488nm. The functionality of the protocol was verified by using the relative brightness in the area where biotin drops were delivered. This can be explained from the binding of streptavidin labeled with Alexa fluorophore to biotin which results to higher brightness as shown in Fig. 4.1.

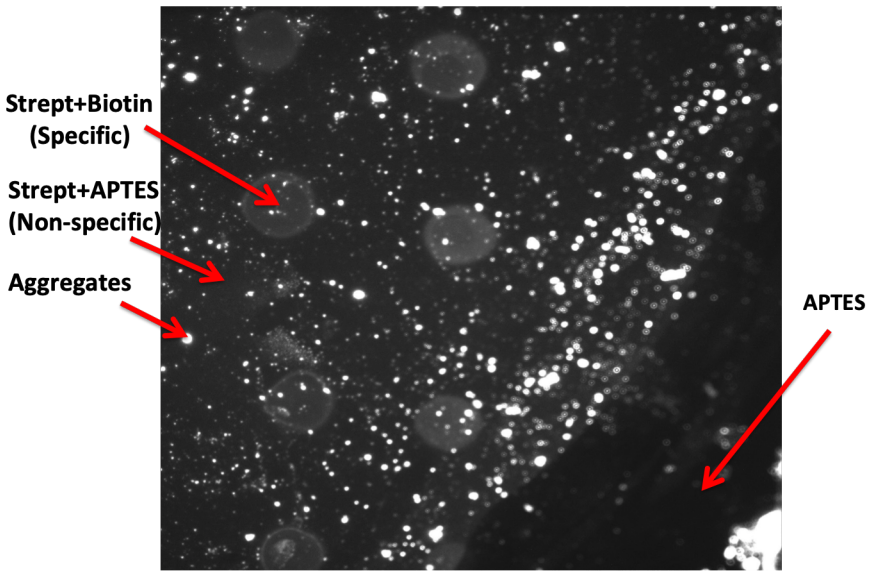

Figure 4.1: Fluorescent visualization of specific binding between avidin and biotin using a FITC filter. The bright spots correspond to biotin-avidin pairs. The less bright region indicates some amount of non specific binding.

The glass slide includes three main distinct areas. The brighter spots correspond to the specific binding between the labeled avidin and biotin. Around these spots, however, a less bright region can be observed. This is the result of the non specific binding of avidin directly to the APTES layer on the slide. Being able to estimate and quantify the non specific binding is one of the greatest challenges in label-free assays since it can become a source of false positive results. More advanced functionalization protocols can be employed blocking any non-specific binding [10]. However, this cancellation of the background signal can be achieved with on chip techniques without requiring complex chemistry that could increase the cost. More details about non specific binding will be discussed in Chapter 5. Finally the darkest area corresponds to an APTES only functionalized surface.

4.2 Microfluidic Delivery Mechanism

Functionalizing statically the surface results to numerous protein aggregates all over the area covered by streptavidin, as seen in Fig. 4.1. The size of these bright spots would strongly interfere with the real time signal obtained from the molecular kinetics since it would affect both the quality of the surface chemistry as well as the surface sensitivity of the platform. Therefore, this suggests that both functionalization and kinetic experiments need to be carried out in a more dynamic way, indicating the requirement for a microfluidic channel network delivering the solution under test.

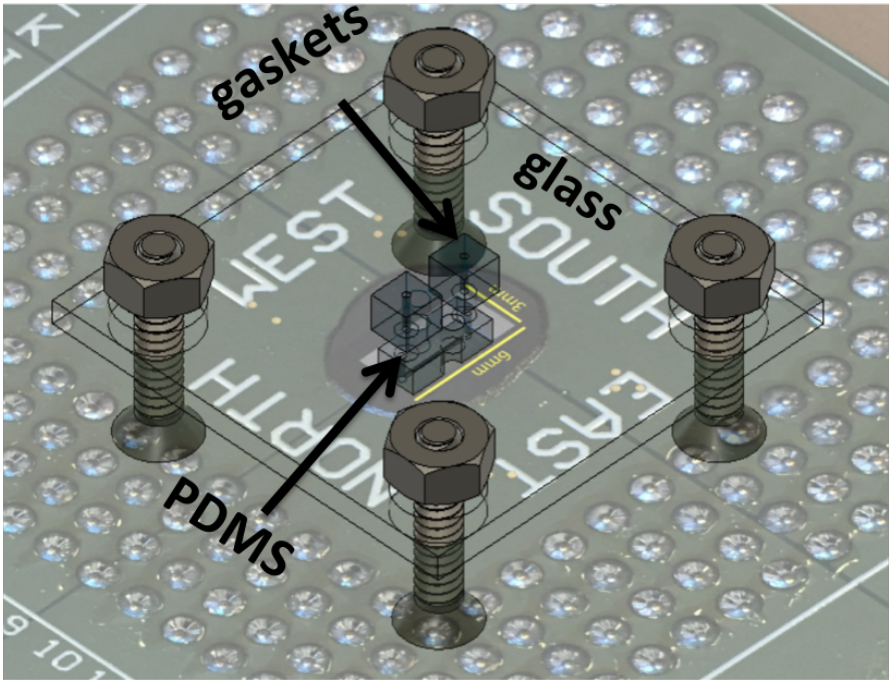

Figure 4.2: The attachment of the microfluidic device on the chip is achieved through mechanical pressure using glass, avoiding any fluidic leakage. Holes are cut in the PDMS for the inlet/outlet ports and the fiber access areas.

Several challenges had to be faced during the design of a channel network compatible to our process and the size of the die. First, microfluidic devices at the size of the chip had to be fab-

ricated. This created challenges for manufacturing the PDMS structures guiding the fluid as well as patterning the fluidic inlet/outlet ports and cuts for the fiber access. Furthermore bonding of the PDMS core device on the chip should not require any extra chemical processing that could affect the surface chemistry applied for protein coupling. This suggested that the attachment of the microfluidic device on the chip should be done through mechanical pressure, thus preventing any fluidic leakage. Fig. 4.2 shows the PDMS layer clamped on the CMOS chip only through mechanical pressure, avoiding the need for irreversible chemical bonding.

The core of the microfluidic design, Fig. 4.3, consists of a bottom PDMS layer of 5.2mm x 2mm mounted on a 6mm x 3mm CMOS processor chip with monolithically integrated photonic I/O rows. Its low footprint allows miniaturization of the CMOS die and coupling access to other photonic structures for different applications. In this chip, ring filter banks with doped MRRs of 5um radius, 10k Q and 100mm pitch were utilized as the sensing sites. Each row consists of 11 rings that can be used as sensing or reference devices. The microfluidic channel covers a sensing ring in the filter row, whereas the rest of the rings can be used as references for cancelling any shifts from ambient temperature changes or pressure.

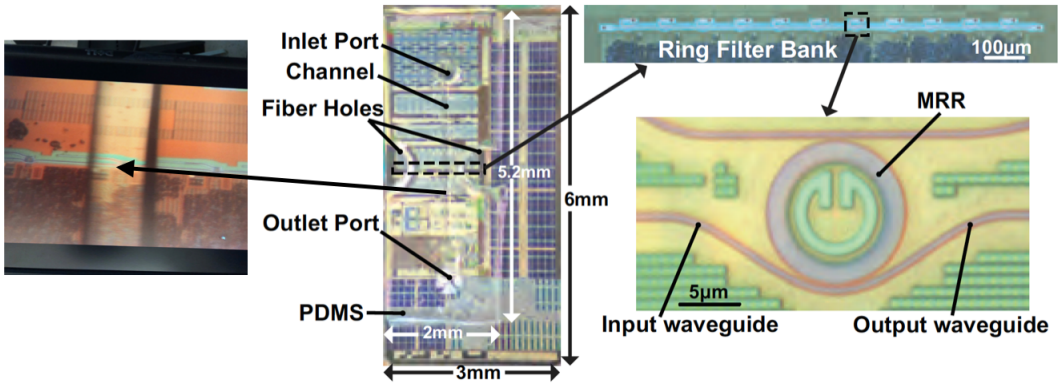

Figure 4.3: PDMS device mounted on the fully Si-substrate released functional processor die, with holes drilled to allow fiber and fluidic access. A ring filter bank is used as the testing site, with 5um radius MRRs for sensing and drift cancellation. A 100um wide channel covers the sensing ring.

This report presents the first version of microfluidics designed for the preliminary kinetic experiments in a fully integrated platform. As it will be discussed in Chapter 5, this design sets some restrictions on the repeatability of these tests, mainly due to the single channel structure. Furthermore, a unique channel covering a single ring does not allow the exposure of any reference sensors under the same environmental conditions, since the rest of the rings are covered by PDMS. Therefore, we cannot extract any precise information of the non specific binding or any other offset shift that can occur from ambient temperature or pressure changes. More advanced microfluidic designs solving several of the aforementioned challenges will be introduced and designed in the future.

Chapter 5

Experimental Results

5.1 Bulk sensitivity

In this chapter, the preliminary experimental results of evanescent field sensing in 45nmRFSOI process will be presented. The goal of these experiments is to first have a proof of concept that this commercially scaled platform can support label free biosensing. Second, these results will verify the modeling and simulation results presented in previous chapters.

The first section examines the bulk sensitivity of the platform. As it was defined in chapter 2, bulk sensitivity is related to the response of the sensor to a uniform and homogeneous change of the cladding material. In order to ensure that the cladding RI change will exceed the evanescent length, large drops of different RI optical oils were spotted on top of the sensors, as shown in 5.1. The estimated thickness of the drop is about 20um. In Fig. 5.2 the resonant shift of the sensors is shown for the different RI oils tested oils in a range of 1.3 to 1.7 with a step of 0.1. An average bulk sensitivity of 5nm/RIU was measured, which is in close agreement with simulation results in Lumerical Mode Solutions.

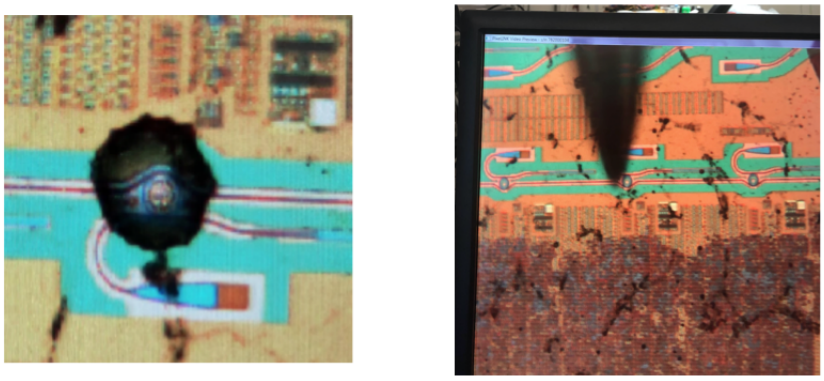

Figure 5.1: Optical oil drops spotted on RRs for bulk sensitivity measurements. The diameter of the drops delivered with a 30 type needle gauge is 20um, therefore fully covering the 5um radius rings.

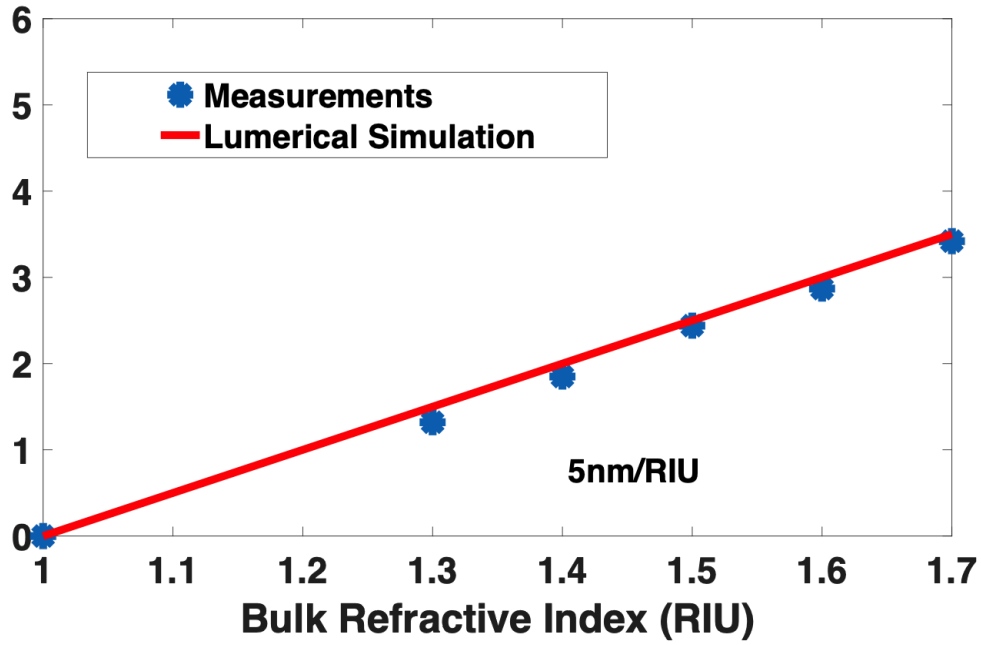

Figure 5.2: Bulk Sensing Sensitivity of the 45nm RFSOI platform.

5.2 Real time kinetics

The surface sensing performance of the chip was evaluated through the molecular interactions between biotin, acting as the probe molecule functionalized over the released BOX surface and streptavidin as the target molecule. In Fig. 5.3, the experimental setup used to demonstrate the sensitivity of the platform is shown. A tunable laser (SANTEC TSL-510) performs multiple scans of the ring row's through port transfer function at a scanning rate of 1min/scan and a step of 5pm while the output power is measured with a power meter (Agilent 8164B).

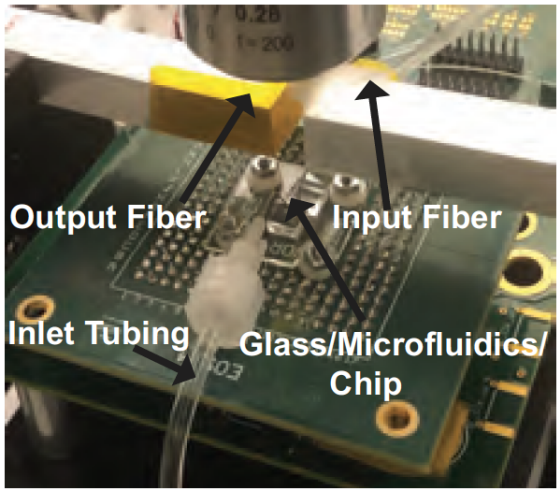

Figure 5.3: Experimental setup with coupled fiber optics and microfluidics.

After the substrate release, the chip was first dip coated for 3 minutes in a 2% APTES (aminosilane)-ethanol solution. A resonant shift of 320pm was observed for the sensing ring. This indicates the presence of 10nm thin layer, based on the layer thickness sensitivity $\frac{\partial \Delta \lambda_r}{\partial t}$ found with FDE simulations, where t is the layer thickness on top of the BOX, and λ_r is the MRR's resonant wavelength. A 3mM biotin-PBS solution was then flowed through the microfluidic channel for 10 hours, to functionalize the sensor with the receptor molecules. The resulting residual shift was 150pm after washing the chip off with deionized (DI) water. The binding between biotin and streptavidin was tested with three different concentrations of streptavidin-PBS solutions flowing through the

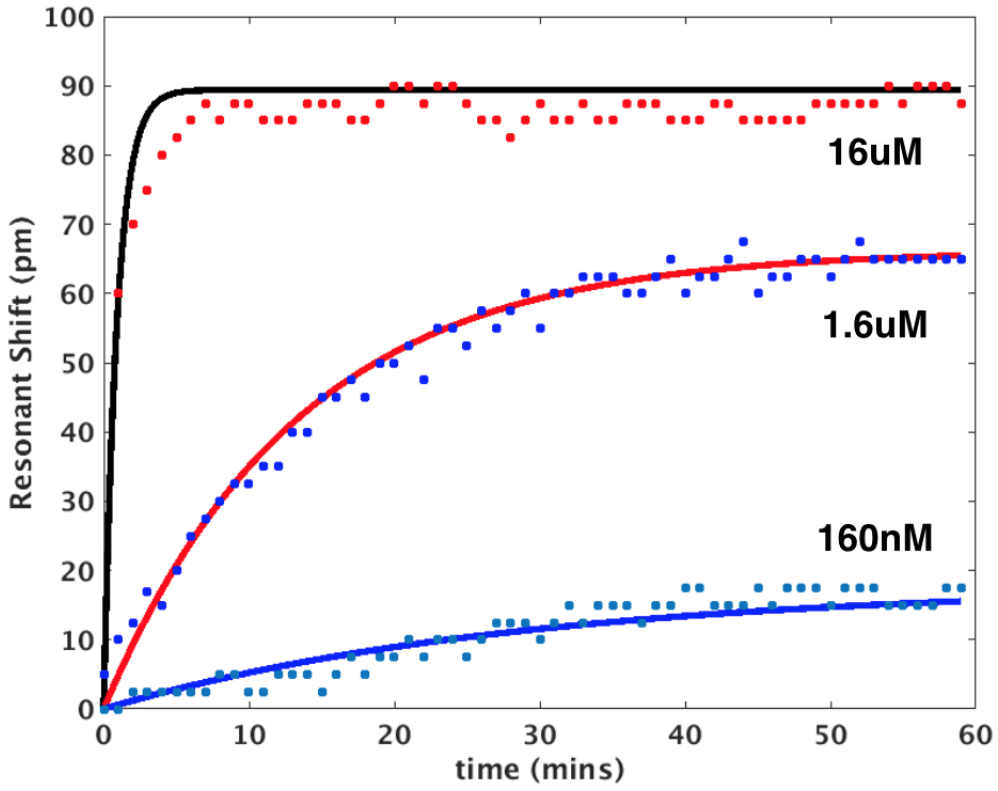

Figure 5.4: Real time resonant shift of biotin-streptavidin binding for different streptavidin concentrations. Solid lines represent the fitted binding curves from the kinetics molecular equation.

channel. Fig. 5.4 shows the real time resonant shift of the functionalized MRR for the different solutions tested [21].

The binding curves are fit to standard pseudo-first order kinetics equation governing protein binding [10], given by:

$$\frac{d[AB]}{dt} = k_a[A][B] - k_d[AB] \tag{5.1}$$

where $[AB]$ is the concentration of the binding pairs between A and B, $[A]$ is the target molecule concentration that we want to determine and $[B]$ is the concentration of the unbound molecules of B that acts as a receptor for target A. The association and dissociation rates are given by k_a $(\frac{1}{Ms})$ and k_d $(\frac{1}{s})$ respectively. If we assume the change in the effective index and the wave-

Table 5.1: Initial binding slope vs Avidin concentration

Avidin Concentration (uM)	Initial Slope
160nM	$1\frac{pm}{min}$
1.6uM	$5\frac{pm}{min}$
16uM	$95\frac{pm}{min}$

length shift to be proportional to the concentration of bound molecules on the top of the sensor then (5.1) can be expressed in the resonant shift domain as follows:

$$\frac{d\Delta\lambda_r(t)}{dt} = k_a[A]A_{area}[B_{max}]S - (k_a[A] + k_d)\Delta\lambda(t) \tag{5.2}$$

where $\Delta\lambda_r$ is the real time resonant shift of the ring, A_{area} is the active area of the functionalized ring for protein binding, $[B_{max}]$ is the initial concentration of the receptor molecules, $[A]$ is the target analyte concentration and S the sensitivity of the ring ($\frac{nm}{molecule}$).

The initial binding slope $\frac{d\Delta\lambda_r(t)}{dt}$ at t=0 can be found by the kinetics equation in the resonant shift domain if we assume that initially $\Delta\lambda_r(t=0) = 0$. Therefore, we can write:

$$\text{Slope} = k_a[A]A_{area}[B_{max}]S \tag{5.3}$$

This shows that the initial slope scales linearly with the initial receptor molecule concentration $[B_{max}]$, the sensitivity S and the concentration of the target analyte $[A]$. Furthermore, it is strongly dependent on the affinity rate constant k_a of the reaction under test.

From the real time kinetics obtained in Fig. 5.4 the effect of streptavidin concentration on the initial binding slope is clear. For higher avidin concentrations the binding curve is faster. Table 5.1 shows the initial slope for different avidin concentrations. The experiments for $160nM$ and $1.6uM$ were done sequentially. This can explain the reduced scaling of the slope at $1.6uM$, which is not linearly increased by 10 times. After the first experiment, some of the binding spots have

been covered by avidin, resulting to a lower number of receptor molecules available for binding in the next experiment. Since the receptor concentration linearly affects the initial binding slope, the measured slope for the $1.6uM$ avidin concentration is lower than expected. However, the experiment for $16uM$ avidin shows that the initial slope is approximately x100 larger than the $160nm$'s slope, which agrees with the predicted linear behavior from the kinetics equation. The steady state shift is also indicative of the target analyte's concentration. A shift of 100pm was measured for the $16uM$ avidin concentration, corresponding to a uniform layer of streptavidin of about 3nm, based on Lumerical simulations.

At this point we should note that based on the simulated surface sensitivity from Lumerical and the used receptor (biotin) and target (avidin) concentrations, the binding slope is expected to be larger. However this slower kinetic behavior can be attributed to the microfluidic channel network. Specifically the relatively large flow rate of the syringe pump (20ul/min) created bubbles during the experiment. The time needed to remove them delayed testing and the fluidic status was switching between a static and a dynamic mode that could slow down the binding slope.

From this preliminary set of real time kinetics in 45RFSOI process some critical testing issues need to be addressed in the future. Residual ambient temperature fluctuations can be observed from the binding curve. The main reason for that is the different cladding material to which sensing and reference rings are exposed. Reference rings are under PDMS, which has a more negative thermo-optic coefficient than the aqueous cladding environment of the sensing rings. Therefore any ambient temperature fluctuations will result to different wavelength shifts for the sensing and reference rings. These wavelength shift offsets can be further reduced by exposing the rings to the same cladding environment.

The exposure of just the sensing rings to the testing solution restricts us from drawing any conclusions regarding non specific binding. Any binding between molecules other than the target analytes (streptavidin) and the immobilized receptors will create a signal that is the result of a non specific interaction. This effect can be eliminated either by some extra blocking steps in the surface chemistry protocol that will limit these non specific interactions or by exposing the

functionalized (sensing) and reference ring to the same buffer solution. Having the sensors under the same testing solution will help us extract a differential shift that will be indicative of just the specific binding between the target analyte and its biorecognition molecule. The common mode term of the sensing and reference shift will provide information about ambient temperature or pressure changes and mostly non specific binding. This uniform exposure can be achieved with a more advanced microfluidic technique, the laminar flow [22]. As shown in Fig. 5.5, two sensors, a sensing and a reference ring are in the same channel, thus exposed to the same testing solution, ensuring a more effective cancellation of the common mode terms.

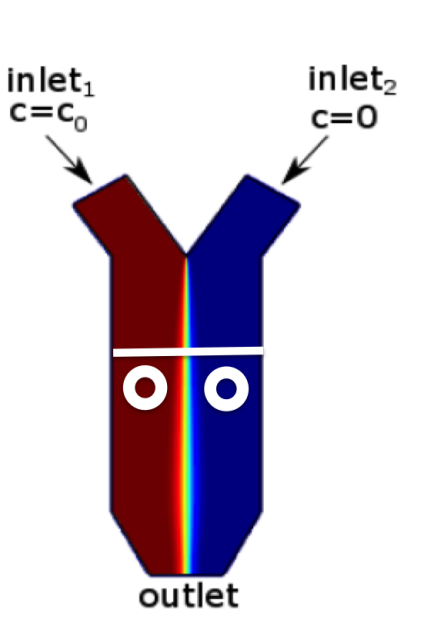

Figure 5.5: Laminar Flow scheme for similar exposure of sensing and reference ring to environmental conditions [22].

Chapter 6

Conclusion

6.1 Summary

This report demonstrated the first label free photonic biosensor in a commercial, scaled CMOS zero-change electronic photonic platform, opening the pathway to the first Lab-on-Chip system with nanophotonic sensing and advanced electronics on a single die. In order to prove the feasibility of a fully integrated electronic-photonic platform for label free biosensing, a detailed analysis of all the critical components of the system was needed. In chapter 2, the operating principle of a widely used resonant structure, the ring resonator, was analyzed and some of its critical spectral design parameters were introduced. The effect of the quality factor on the sharpness of the resonant slope was highlighted and two types of sensitivity, both intrinsic and photonic were defined. Next, the potential of the 45nm CMOS platform as a label free sensing platform was investigated and characterized through simulations, using Lumerical. The overall effect of a testing solution was estimated based on this analysis. The offsets introduced by its background were characterized from the the bulk sensitivity of the platform, while shifts generated by molecular bindings were estimated using the surface sensitivity. In light of these simulation results, we approximated the effect of a single binding event in order to get an estimation of the weakest signal generated from

our sensor.

Moving from the device to a system level, Chapter 3 introduces the basic categories of ring based photonic sensing architectures. A mathematical approach of sensitivity is presented for a single RR and the RAMZI interferometric architecture. Using this analysis we set the basis for the specifications of a biophotonic system monitoring real time kinetics. However, both of these intensity based schemes lack of the ring's phase information that could significantly improve the robustness to any power fluctuations. Therefore, we briefly demonstrate some more advanced photonic systems which can detect phase instead of amplitude.

One of the most fundamental parts of a label free sensing system is the interface between photonic sensors and biology. Chapter 4 aims to present a simplified version of the surface chemistry needed for functionalizing a label free sensor. Using fluorescence as a verification protocol we managed to show the functionality of a simple protocol that can be applied to our platform. This is a first promising step required to prove the feasibility of our fully integrated process for supporting label free sensing technology. Next, we focused on different ways of delivering fluid on our sensor. The first one is based on the static delivery of droplets. The disadvantages of this technique were obvious from the functionalization results, since the static nature of the fluidic delivery resulted to many protein aggregates that could interfere with our kinetic measurements. Therefore, emphasis was given on a more dynamic way of delivering testing solutions using microfluidic devices. However being able to fabricate a device compatible with the requirements of a die in the 45nm process was a challenge. Liquid leakage suppression and size were the main issues we had to face in order to have a functional microfluidic device in our integrated platform. This fabrication work resulted to a single channel microfluidic network used for the real time kinetic experiments presented in the next chapter.

Chapter 5 presented some preliminary results of label free sensing in a commercial CMOS 45nm process. First, the bulk sensitivity results were shown and strong agreement was found with Lumerical Simulations. The second part of this chapter showed real time kinetics of molecular interactions for the first time in a fully integrated platform. The binding pair of biotin and strepta-

vidin was used in order to draw clear conclusions regarding the efficiency of the surface chemistry and the fluidic delivery system. These promising results, however, show that there is significant room for future improvements. Having a single channel limits at a large amount the repeatability of these experiments, the number of sensing sites we test, as well as the precision of the kinetics data we get. Future microfluidic designs will address these challenges.

This work as a whole sets the basis for a first of its kind fully integrated system with biophotonic sensing and readout processing on the same die. A theoretical analysis of the sensing capabilities of this platform along with preliminary experimental results helped us build a solid background in order to move towards a fully integrated direction in the future.

6.2 Future Work

A fully integrated system with nanophotonic sensing and signal processing on the same die will reduce cost and enable self-contained point-of-care devices that are needed in health-care applications. This can be implemented by integrating and packaging the components analyzed in this report into one system. However, one of the contributions of this report was also to highlight some current limitations and point to future directions of improvements. Starting from the intrinsic sensitivity of our platform, we are going to verify the significant boost in performance that we get with a reduced BOX thickness. This will include experimentation with different SiO2 etching techniques in order to make sure that post etching functionality of both electronics and photonics is preserved. At the same time more sensitive RRs tailored for sensing applications rather than modulators will be designed. The use of ring modulators in this report was able to achieve a proof of the label free sensing concept, however it limited the minimum detectable signal (MDS) we could get. Higher quality factor rings were previously demonstrated in our platform [19], setting a promising direction for future photonic designs that will significantly lower the MDS. One of the main challenges not discussed in this report is a low noise readout processing system. By leveraging high precision circuit techniques combined with more robust phase detection architectures

we hope to not only unlock the door to fully integrated systems but also enhance the achieved SNR. In order to do so, a thorough circuit analysis needs to be performed in order to evaluate the dominant noise sources and target specific circuit architectures. At the same time, a more detailed analysis of the phase detection schemes mentioned in this report is required in order to emphasize the significance and advantages of these architectures compared to intensity based topologies. Finally, significant improvements in the surface chemistry and microfluidics are strongly desired and targeted in the future. As it was highlighted in the report, cancellation of non specific binding and ambient common mode errors was limited in a single channel design. Using better microfluidic techniques and more automated fabrication processes like 3D printing, we can scale the number of testing channels and achieve a high fabrication yield with a small turnaround time.

Bibliography

[1] B. T. Cunningham, *Label-Free Optical Biosensors: An Introduction,* Cambridge University Press, UK 2009.

[2] Sakamoto, S.; Putalun, W.; Vimolmangkang, S.; Phoolcharoen, W.; Shoyama, Y.; Tanaka, H.; Morimoto, S. *Enzyme-Linked Immunosorbent Assay for the Quantitative/qualitative Analysis of Plant Secondary Metabolites.* J. Nat. Med. 2018, 72, 32–42. DOI:10.1007/s11418-017-1144-z.

[3] Arlett JL, Myers EB, Roukes ML. *Comparative advantages of mechanical biosensors.* Nature Nanotech. 2011;6:203–215.

[4] J. S. Daniels, *"An integrated impedance biosensor array,"* Ph.D. dissertation, Dept. Elect. Eng. Stanford Univ., Stanford, CA, USA, 2010.

[5] A. Manickam, A. Chevalier, M. McDermortt, A. D. Ellington, and A. Hassibi, *"A CMOS electrochemical impedance spectroscopy biosensor array for label-free biomolecular detection,"* in Proc. IEEE Int. Solid- State Circuits Conf., 2010, pp. 130–131.

[6] A. L. Washburn, L. C. Gunn, and R. C. Bailey, *"Label-free quantitation of a cancer biomarker in complex media using silicon photonic microring resonators,"* Anal. Chem., vol. 81, no. 22, pp. 9499–9506, Nov. 2009.

[7] E. Luan, et al., *"Sub-wavelength multi-box waveguide-based label-free sensors,"* Integrated Optics: Devices, Materials, and Technologies XXII , SPIE 10535,15 (2018).

[8] C. Sun, et al., *"Single-chip microprocessor that communicates directly using light,"* Nature 528, 534–538 (2015).

[9] Bogaerts, W. et al. *Silicon microring resonators.* Laser Photonics Rev. 6, 47–73 (2012).

[10] K. DeVos, *Label-Free Silicon Photonics Biosensor Platform with Microring Resonators,* PhD Thesis, Ghent University, Belgium (2010).

[11] Yoshie, T.; Tang, L.; Su, S.Y. *Optical microcavity: Sensing down to single molecules and atoms.* Sensors 2011, 11, 1972–1991.

[12] J. Loud, S. Perper, R. Twomey, and S. Clarke, *"Characterization of Anti-Nuclear Antibody (ANA) Signatures in Murine Models of Lupus Using Genalyte Maverick Technology,"* in ARTHRITIS & RHEUMATOLOGY, 2015, vol. 67.

[13] M. Iqbal, et al., *"Label-Free Biosensor Arrays Based on Silicon Ring Resonators and High-Speed Optical Scanning Instrumentation,"* IEEE J. Sel. Top. Quantum Electron., 16(3), 654–661 (2010).

[14] F. Vollmer and L. Yang, *"Label-free detection with high-Q microcavities: a review of biosensing mechanisms for integrated devices,"* Nanophotonics, vol. 1, no. 3–4, pp. 267–291, Dec. 2012.

[15] A. L. Washburn, M. S. Luchansky, A. L. Bowman, and R. C. Bailey, *"Quantitative, Label-Free Detection of Five Protein Biomarkers Using Multiplexed Arrays of Silicon Photonic Microring Resonators,"* Anal. Chem., vol. 82, no. 1, pp. 69–72, 2010.

[16] A. M. Armani, R. P. Kulkarni, S. E. Fraser, R. C. Flagan, and K. J. Vahala, *"Label-free, single-molecule detection with optical microcavities,"* Science, vol. 317, no. 5839, pp. 783–787, Aug. 2007.

[17] J. Witzens and M. Hochberg, *"Optical detection of target molecule induced aggregation of nanoparticles by means of high-Q resonators,"* Opt. Express, vol. 19, no. 8, pp. 7034–7061, Apr. 2011.

[18] M. Terrel, M. J. F. Digonnet, and S. Fan, *"Ring-coupled Mach-Zehnder interferometer optimized for sensing,"* Appl. Opt. 48(26), 4874–4879 (2009).

[19] J. S. Orcutt, et al., *"Open foundry platform for high-performance electronic-photonic integration."* Opt. Express 20(11), 12222–12232 (2012).

[20] R. A. Soref and B. R. Bennett, *Electrooptical effects in silicon* IEEE J. Quantum Electron., vol. QE-23, no. 1, pp. 123–129, 1987.

[21] Adamopoulos C, Gharia A, Niknejad A, Anwar M, Stojanović V., *"Electronic-Photonic Platform for Label-Free Biophotonic Sensing in Advanced Zero-Change CMOS-SOI Process,"* Conference on Lasers and Electro-Optics, OSA; 2019. p. JW2A.81.

[22] P. Popescu, *"An Optofluidic Ring Resonator Platform for Rapid and Robust Sensing,"* Ph.D. dissertation, Dept. of Applied Physics. California Institute of Technology, Pasadena, CA, USA, 2017.